RESEARCH ARTICLE

Brain Iron and Metabolic Abnormalities in C19orf12 Mutation Carriers: A 7.0 Tesla MRI Study in Mitochondrial Membrane Protein–Associated Neurodegeneration

Petr Dusek, MD,[1,2] Ralf Mekle, PhD,[3,4] Marta Skowronska, MD,[5] Julio Acosta-Cabronero, PhD,[6] Till Huelnhagen, PhD,[7]
Simon Daniel Robinson, PhD,[8] Florian Schubert, PhD,[3] Marcus Deschauer, MD,[9] Antje Els, BSc,[7]
Bernd Ittermann, PhD,[3] Gudrun Schottmann, MD,[10] Vince I. Madai, PhD,[4,11] Friedemann Paul, MD,[10]
Thomas Klopstock, MD,[12,13,14] Tomasz Kmiec, MD,[15] Thoralf Niendorf, MD,[7] Jens Wuerfel, MD,[10,16] and
Susanne A. Schneider, MD, PhD[17*]

[1]Department of Neurology and Centre of Clinical Neuroscience, Charles University, 1st Faculty of Medicine and General University Hospital in Prague, Prague, Czechia
[2]Department of Radiology, Charles University, 1st Faculty of Medicine and General University Hospital in Prague, Prague, Czechia
[3]Physikalisch-Technische Bundesanstalt (PTB), Braunschweig and Berlin, Germany
[4]Center for Stroke Research Berlin (CSB), Charité Universitätsmedizin Berlin, Berlin, Germany
[5]2nd Department of Neurology, Institute of Psychiatry and Neurology, Warsaw, Poland
[6]Wellcome Centre for Human Neuroimaging, UCL Institute of Neurology, University College London, London, United Kingdom
[7]Berlin Ultrahigh Field Facility (B.U.F.F.), Max Delbrück Center for Molecular Medicine in the Helmholtz Association (MDC), Berlin, Germany
[8]High Field MR Centre, Department of Biomedical Imaging and Image-guided Therapy, Medical University of Vienna, Vienna, Austria
[9]Department of Neurology, Technical University Munich, Munich, Germany
[10]NeuroCure Clinical Research Center and Experimental and Clinical Research Center, Max Delbrueck Center for Molecular Medicine and Charité-Universitaetsmedizin Berlin, Berlin, Germany
[11]Department of Neurosurgery, Charité Universitätsmedizin Berlin, Berlin, Germany
[12]Department of Neurology with Friedrich-Baur-Institute, Ludwig-Maximilians-University of Munich, Munich, Germany
[13]German Center for Neurodegenerative Diseases (DZNE), Munich, Germany
[14]Munich Cluster for Systems Neurology (SyNergy), Munich, Germany
[15]Department of Neurology and Epileptology, The Children's Memorial Health Institute, Warsaw, Poland
[16]Medical Image Analysis Center and Department Biomedical Engineering, University Basel, Basel, Switzerland
[17]Neurology Department, Ludwig Maximilians-University of Munich, Germany

ABSTRACT: Background: Mitochondrial membrane protein-associated neurodegeneration is an autosomal-recessive disorder caused by *C19orf12* mutations and characterized by iron deposits in the basal ganglia.

Objectives: The aim of this study was to quantify iron concentrations in deep gray matter structures using quantitative susceptibility mapping MRI and to characterize metabolic abnormalities in the pyramidal pathway using ^{1}H MR

*Correspondence to: Prof. Susanne A. Schneider, Department of Neurology, University of Munich, Marchioninistraße 15, 81377 Munich, Germany; E-mail: susanne.schneider@med.uni-muenchen.de; or Dr. Jens Wuerfel, MD, MIAC AG, Marktgasse 8, 4051 Basel, Switzerland; E-mail: ceo-office@miac.ch

Drs. Dusek and Mekle contributed equally as first authors.

spectroscopy in clinically manifesting membrane protein-associated neurodegeneration patients and asymptomatic *C19orf12* gene mutation heterozygous carriers.

Methods: We present data of 4 clinically affected membrane protein-associated neurodegeneration patients (mean age: 21.0 ± 2.9 years) and 9 heterozygous gene mutation carriers (mean age: 50.4 ± 9.8 years), compared to age-matched healthy controls. MRI assessments were performed on a 7.0 Tesla whole-body system, consisting of whole-brain gradient-echo scans and short echo time, single-volume MR spectroscopy in the white matter of the precentral/postcentral gyrus. Quantitative susceptibility mapping, a surrogate marker for iron concentration, was performed using a state-of-the-art multiscale dipole inversion approach with focus on the globus pallidus, thalamus, putamen, caudate nucleus, and SN.

Results and Conclusion: In membrane protein-associated neurodegeneration patients, magnetic susceptibilities were 2 to 3 times higher in the globus pallidus ($P = 0.02$) and SN ($P = 0.02$) compared to controls. In addition, significantly higher magnetic susceptibility was observed in the caudate nucleus ($P = 0.02$). Non-manifesting heterozygous mutation carriers exhibited significantly increased magnetic susceptibility (relative to controls) in the putamen ($P = 0.003$) and caudate nucleus ($P = 0.001$), which may be an endophenotypic marker of genetic heterozygosity. MR spectroscopy revealed significantly increased levels of glutamate, taurine, and the combined concentration of glutamate and glutamine in membrane protein-associated neurodegeneration, which may be a correlate of corticospinal pathway dysfunction frequently observed in membrane protein-associated neurodegeneration patients. © 2019 The Authors. *Movement Disorders* published by Wiley Periodicals LLC on behalf of International Parkinson and Movement Disorder Society.

Key Words: 7 Tesla MRI; glutamate; magnetic resonance spectroscopy; mitochondrial membrane protein–associated neurodegeneration (MPAN); neurodegeneration with brain iron accumulation (NBIA); quantitative susceptibility mapping, iron

The syndromes of neurodegeneration with brain iron accumulation (NBIA) are a group of progressive hypo- and/or hyperkinetic movement disorders associated with pathological excess of iron deposition in the brain, particularly affecting the basal ganglia, mainly the globus pallidus (GP).[1] Of these, mitochondrial membrane protein-associated neurodegeneration (MPAN) is a rare form caused by mutations in the *C19orf12* gene, which encodes a protein with a presumed function in lipid metabolism.[2-4] Symptoms include progressive movement disorders, spasticity, neuropathy, cognitive dysfunction, and optic nerve atrophy.

Iron accumulation in NBIA syndromes can be detected as a prominent hypointensity in T2- and T2*-weighted (T2w/T2*w) MRI.[1] In MPAN, brain MRI typically shows focal abnormalities consistent with increased iron levels in the GP and SN.[2] In older patients with long disease duration and/or late onset, iron deposits were observed also in the putamen and caudate nucleus.[5,6] Additionally, white matter (WM) hyperintensities primarily affecting the periventricular region,[7] and cortical hypometabolism on brain fluorodeoxyglucose PET,[5] have also been described. Interestingly, iron deposition in MPAN follows a similar pattern as in pantothenate-kinase–associated neurodegeneration (PKAN), where the predominant sites of iron accumulation are also the GP and SN, despite substantial differences in clinical symptoms. Dystonia predominates in PKAN,[8] whereas MPAN patients typically manifest with spastic paresis,[9] suggesting involvement of the corticospinal pathway in addition to basal ganglia disturbances.

To date, the vast majority of neuroimaging studies in MPAN have utilized routine clinical MR scans.[7] Iron-sensitive quantitative MRI measures have only been reported for a single MPAN case, showing 3 times higher paramagnetism in GP and SN compared to controls.[10] To address the lack of quantitative data, we applied the technique of quantitative susceptibility mapping (QSM)[11] with ultrahigh field MRI to study the iron concentrations in the cerebral deep gray matter in MPAN.

In addition, we investigated the neurochemical profile in the precentral/postcentral WM using single-volume ^{1}H MR spectroscopy (MRS) on the earlier hypothesis that metabolic abnormalities in the corticospinal pathway might explain the pyramidal symptoms characteristically present in MPAN patients.[12] MRS benefits 2-fold from acquisitions at higher static magnetic field strength (B_0): through enhanced sensitivity and increased spectral resolution.[13,14] In addition to MPAN patients, *C19orf12* heterozygotes were also studied on the earlier hypotheses that (subtle) clinical and/or imaging abnormalities are present in this cohort, and the latter are detectable with current MRI technology.

In summary, the aims of our study were to (1) quantify iron concentration and volume of the deep gray matter nuclei and (2) characterize underlying metabolic changes using ^{1}H MRS in the corticospinal pathway, both in MPAN patients and heterozygous *C19orf12* mutation carriers relative to healthy controls.

Participants and Methods

Participants

The study was approved by the local ethics committees, and participants gave written informed consent before the study. Patients were identified through routine clinical care and through the international NBIA

registry as set up in the "Treat Iron-Related Childhood-Onset Neurodegeneration" (TIRCON) project (www.TIRCON.eu).

Four MPAN patients (3/1 male/female; mean age: 21.0 ± 2.9 [interval, 19–24] years) and 9 heterozygous gene mutation carriers (4/5 male/female; mean age: 50.4 ± 9.8 [interval, 36–63] years) were assessed (Table 1). Of note, scans from 2 additional MPAN patients and 1 heterozygous carrier had to be excluded from the analysis because of severe motion artifacts. Nineteen healthy volunteers (10/9 male/female; mean age: 41.2 ± 14.9 [interval, 18–67] years) were recruited for imaging comparison. The broad age range of the healthy control group was set to (1) match both young MPAN and older healthy adult heterozygote groups and (2) calculate a regression equation for the dependence of iron concentration on age in healthy population so that changes in the heterozygous gene carrier group could be appropriately contextualized. All study subjects were whites.

MR spectra were acquired in 3 MPAN patients (1 patient, subject 4, voluntarily withdrew from the session before completion), 9 heterozygotes, and 9 controls (with a mean age matched to the heterozygote group); 1 control subject was excluded from MRS analysis because of poor data quality.

All participants were neurologically examined with focus on the presence (patients) or absence (asymptomatic mutation carriers and controls) of movement disorder abnormalities.

MRI Data Acquisition

MR images were acquired on a Magnetom 7.0 Tesla (T) whole-body MR system (Siemens Healthcare, Erlangen, Germany), using a 24-channel receive head coil (Nova Medical, Wilmington, MA). The MRI protocol included a three-dimensional (3D) magnetization-prepared rapid acquisition with gradient echo scan (MPRAGE; repetition time [TR] = 2,300 ms, echo time [TE] = 2.98 ms; inversion time = 900 ms, flip angle [FA] = 5 degrees, spatial resolution $1.0 \times 1.0 \times 1.0$ mm^3, bandwidth = 238 Hz/pixel) for anatomical imaging and guiding MRS volume positioning, a two-dimensional (2D) fast low angle shot gradient echo scan (GRE; TR = 1820 ms, eight equidistant TEs from 4.1 to 25.5 ms, FA = 35 degrees, spatial resolution = $0.5 \times 0.5 \times 2$ mm^3, bandwidth = 407 Hz/pixel, 35 slices) for proton-density (PD) and T2*-weighted anatomical imaging; and a 3D flow-compensated GRE scan (TR = 30 ms, TE = 15.3 ms, FA = 30 degrees, spatial resolution = $0.3 \times 0.3 \times 1$ mm^3, bandwidth = 180 Hz/pixel) for QSM.

QSM Postprocessing and Analysis

Phase images from separate radiofrequency (RF) coils were combined offline using a virtual reference coil approach.[15] QSM was processed with the QSMbox software package (https://gitlab.com/acostaj/QSMbox), using a previously validated pipeline for combined single-echo data and the multiscale dipole inversion procedure[16] (regularization parameter λ = 630, default settings otherwise).

MPRAGE images were registered to the GRE magnitude images using SPM12 software (www.fil.ion.ucl.ac.uk). 3D regions of interest (ROIs) defining bilateral GP, SN, caudate nucleus, putamen, and thalamus were manually segmented on coregistered QSM and MPRAGE images using ITK-SNAP 3.6 (www.itksnap.org). Volumes and mean susceptibility values of each ROI were extracted. Susceptibility was obtained after excluding voxels containing large vessels from segmentation masks and corrected by subtracting the value from a homogenous reference region in parietooccipital WM rostral to optic radiation. Volumetric data were adjusted according to the total intracranial volume using the residual method as previously described.[17]

MRS Data Acquisition

For MRS, the volume of interest (VOI) was carefully positioned into the left precentral/postcentral WM beneath the central sulcus. Localized RF calibration was performed, and first- and second-order shims were adjusted using a vendor-supplied algorithm. Subsequently, the linewidth (full width at half-maximum) of an unsuppressed water signal from the VOI was measured to verify the shim settings. Single-volume data were acquired using the spin echo full intensity acquired localized (SPECIAL) MRS technique[13,18] (VOI = $20 \times 20 \times 20$ mm^3, TR/TE = 9000/11 ms, number of averages [NA] = 64, spectral width = 4,000 Hz, and T_{acq} = 512 ms). An unsuppressed water signal from the same VOI was also measured using NA = 4. Full localization in SPECIAL is achieved by combining a slice-selective adiabatic inversion pulse applied in alternate scans with a 2D spin echo module. In addition, six bands of outer volume saturation were interleaved with the variable-pulse power and optimized relaxation delays water suppression scheme[19] to eliminate lipid contaminations.[13] For spectral acquisitions, the reference excitation frequency was shifted upfield 2.3 parts per million (ppm) from the water resonance.

MRS Data Processing and Analysis

MRS data were postprocessed using an in-house MATLAB (The MathWorks, Inc., Natick, MA) program. Processing steps included the combination of signals from multiple RF coil elements,[20] applying the add-subtract scheme inherent to SPECIAL, frequency drift correction of the individual fully localized spectra, and averaging. Metabolite quantification was performed using LCModel[21] with a basis set of 21 simulated metabolites and an experimentally acquired set of macromolecules including lipid signals for improved accuracy.[22] For analysis, the spectral range was set to 0.2 to 4.2 ppm. Eddy current correction within LCModel was enabled, and the unsuppressed water signal from the VOI was used to calculate concentration values.

Resulting in vivo concentrations were corrected for the cerebrospinal fluid content of each VOI after segmenting the T1-weighted MPRAGE images using FSL BET and FAST routines (https://fsl.fmrib.ox.ac.uk).[23]

Statistical Analysis

Statistical analyses were conducted using GraphPad Prism software (version v6.0.7; GraphPad Software Inc., San Diego, CA). Because of the well-known effect of age on cerebral iron concentration and the significant age difference between MPAN patients and heterozygous mutation carriers, each group was compared with different age-matched control groups. Mann-Whitney U tests were performed to cross-sectionally compare MRS and bulk ROI susceptibility values of biallelic and heterozygous C19orf12 mutation carriers and control groups. Given that this study is considered preliminary, corrections for multiple comparisons were not performed. Subsequently, univariate linear regressions were performed to characterize the effects of age on regional mean susceptibilities in heterozygous C19orf12 mutation carriers in contrast to those in healthy controls.

Results

Clinical Information and Visual MRI Analysis

Demographic and clinical data of patients and heterozygotes are shown in Table 1. All patients had clinical signs of corticospinal pathway lesion; disease onset ranged from 8 to 12 years and duration of symptoms from 10 to 13 years. Heterozygous C19orf12 mutation carriers did not exhibit any neurological abnormalities

on examination, except one participant who had mild action tremor (subject 6). Genetic testing with full C19orf12 sequencing revealed homozygous mutations in all patients.

All MPAN patients had pronounced hypointensities on the magnitude images in the GP and SN (Figs. 1 and 2). Subtle hypointensities were also observed in the anterior aspect of the caudate nucleus (Fig. 2). The internal medullary lamina of the GP was apparent on MPRAGE and PD-weighted GRE images of all MPAN patients. Two patients showed cerebellar atrophy, and cortical as well as central atrophy, respectively (subjects 4 and 5; Fig. 1). In addition, one of the heterozygous carriers exhibited unspecific WM lesions (subject 11). MRI findings, including signal in the basal ganglia, in the other heterozygotes were normal on visual inspection.

QSM and Volumetric Analysis

In MPAN patients, bulk magnetic susceptibility in the GP ($P = 0.016$) and SN ($P = 0.016$) was substantially higher compared to controls. In addition, significantly higher magnetic susceptibility was also observed in the caudate nucleus ($P = 0.016$; Figs. 1 and 3). C19orf12 mutation heterozygotes exhibited significantly increased susceptibility in the putamen ($P = 0.003$) and caudate nucleus ($P = 0.001$), whereas susceptibility in the GP, SN, and thalamus was not significantly different from those in controls (Fig. 3; Supporting Information Table S1). Linear regression analysis in healthy controls showed significant positive correlations between age and susceptibility in the putamen ($r^2 = 0.80$; $P < 0.0001$), caudate nucleus ($r^2 = 0.30$; $P = 0.015$), and SN

TABLE 1. Demographic, clinical, and genetic information of MPAN subjects

| ID	Family	Group	Age	Clinical Status	Age at Onset	Genetics
1	Family 1[a]	Het	60	Non-Manif	n/a	c.197-199del3 (p.Gly66del)
2	Family 1[a]	Het	55	Non-Manif	n/a	c.32C>T (p.Thr11Met);
3	Family 2[a]	Het	55	Non-Manif	n/a	c.204-214del11bp (p.Gly69Argfs*10)
4	Family 3[b]	Pat	24	Dysarthria, dystonia, parkinsonism, mild intention tremor, axonal neuropathy	11	c.177-178insG (p.Leu60Alafs10X), homozygous
5	Family 4[c]	Pat	24	Optic nerve atrophy, muscle atrophy, mixed quadruparesis, dysarthria	12	c.204_214del11 (p.Gly69RfsX10), homozygous
6	Family 4[c]	Het	61	Mild intention tremor	n.d.	c.204_214del11 (p.Gly69RfsX10)[d]
7	Family 4[c]	Het	64	Non-Manif	n/a	c.204_214del11 (p.Gly69RfsX10)[d]
8	Family 5[c]	Pat	19	Optic nerve atrophy, dysarthria, leg spasticity with ankle contractions, mild dystonia, wheelchair-bound	8	c.204_214del11 (p.Gly69RfsX10); homozygous
9	Family 5[c]	Het	37	Non-Manif	n/a	c.204_214del11 (p.Gly69RfsX10)[d]
10	Family 5[c]	Het	42	Non-Manif	n/a	c.204_214del11 (p.Gly69RfsX10)[d]
11	Family 6	Het	45	Non-Manif	n/a	c.194G>T
12	Family 7	Pat	19	Optic nerve atrophy, dystonic smile, dysarthia, spastic quadruparesis, pes cavus, gait only with walker	9	c.204-214del11bp (p.G69RfsX10), homozygous
13	Family 7	Het	41	Non-Manif	n/a	c.204-214del11bp (p.G69RfsX10)

[a]Families previously reported by Deschauer and colleagues.[43]
[b]Previously reported by Schottmann and colleagues.[44]
[c]Previously reported by Hartig and colleagues.[2]
[d]Heterozygotes not formally genetically tested, their genotype was deducted from the known mutation in their offspring.
Het, heterozygous; Pat, patient; Non-Manif, nonmanifesting; n/a, not applicable; n.d., no data.
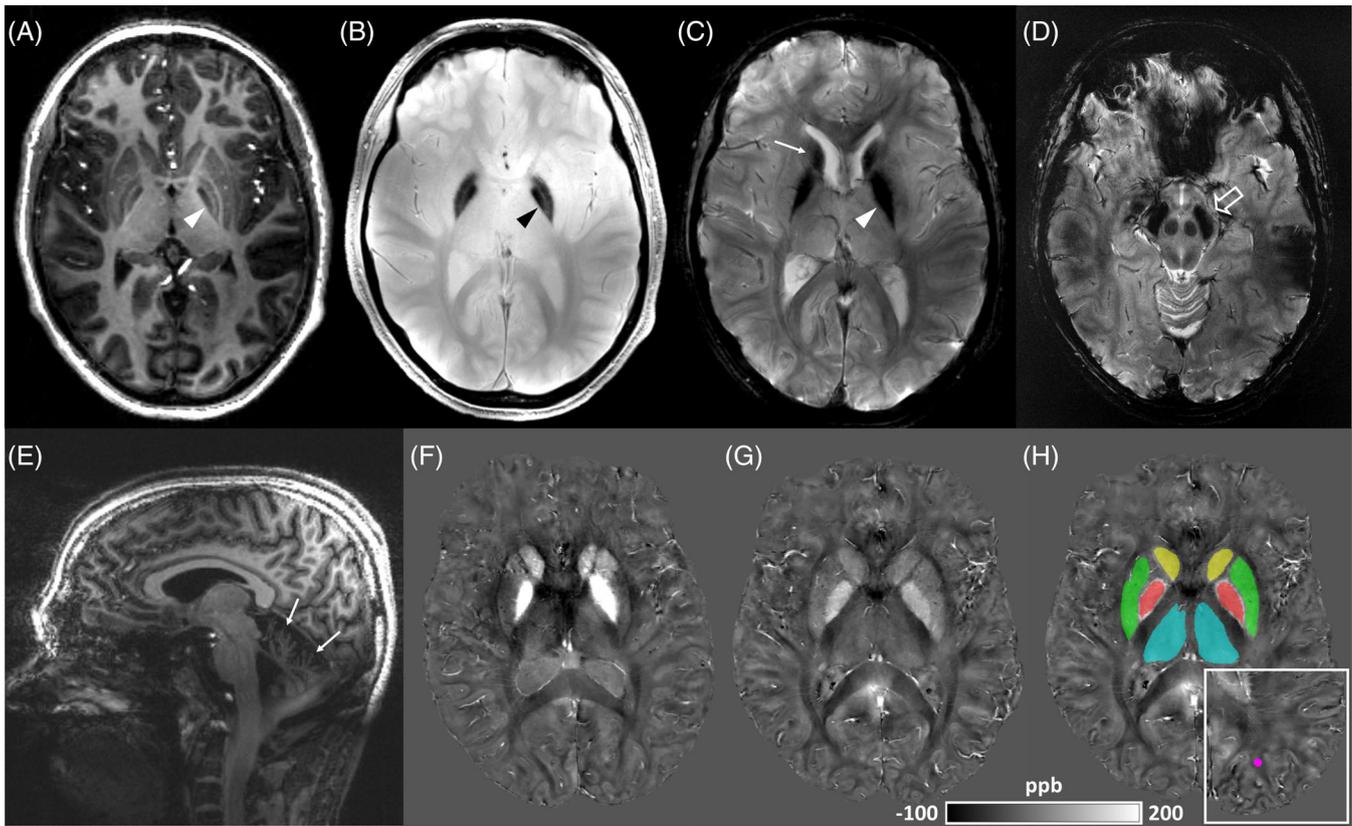
FIG. 1. (A) Axial MPRAGE and (B) short-echo (4.1 ms) 2D GRE images show profound iron deposits in the GP with preservation of internal medullary lamina in an MPAN patient (white and black arrowheads); (C) in the late-echo (19.4 ms) 2D GRE image, the internal medullary lamina is overshadowed by the signal drop attributable to magnetic field inhomogeneities caused by nonlocal sources (white arrowhead); a hypointensity of the caudate nucleus becomes apparent (white arrow); (D) 2D GRE image showing iron deposits in the SN (open arrow); (E) sagittal MPRAGE image demonstrating cerebellar atrophy in an MPAN patient (white arrows); exemplary susceptibility maps (in parts per billion [ppb]) of an (F) MPAN patient and (G) age-matched control; (H) the latter is shown with segmentation mask (caudate nucleus in yellow, putamen in green, GP in red, and thalamus in cyan color); inset shows reference region in parieto-occipital WM on a more rostral slice (in pink). [Color figure can be viewed at wileyonlinelibrary.com]

($r^2 = 0.26$; $P = 0.027$), whereas there were no significant correlations in GP and thalamus. The slope of age-related iron accumulation was not significantly different between healthy controls and heterozygotes. The y-intercept, however, was significantly higher in the putamen ($P < 0.0001$) and caudate nucleus ($P = 0.0006$; Supporting Information Fig. S1) in heterozygotes compared to healthy controls. Volumetric analysis of deep gray matter nuclei did not show any significant differences between *C19orf12* mutation heterozygotes and age-matched controls. In MPAN patients, volumes of the caudate nucleus ($P = 0.016$), putamen ($P = 0.032$), and thalamus ($P = 0.032$)
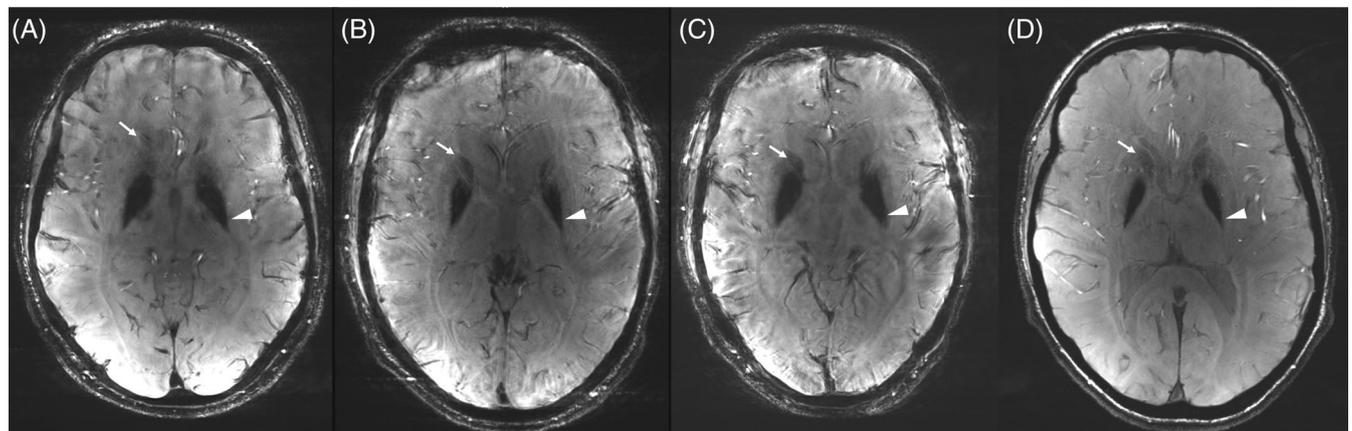
FIG. 2. Axial 3D GRE magnitude images of all MPAN patients at the level of basal ganglia. Profound hypointensities are apparent in the GP (white arrowheads), with less pronounced signal reduction in the head of the caudate nucleus (white arrows). (A) Subject 4, (B) subject 5, (C) subject 8, and (D) subject 12.
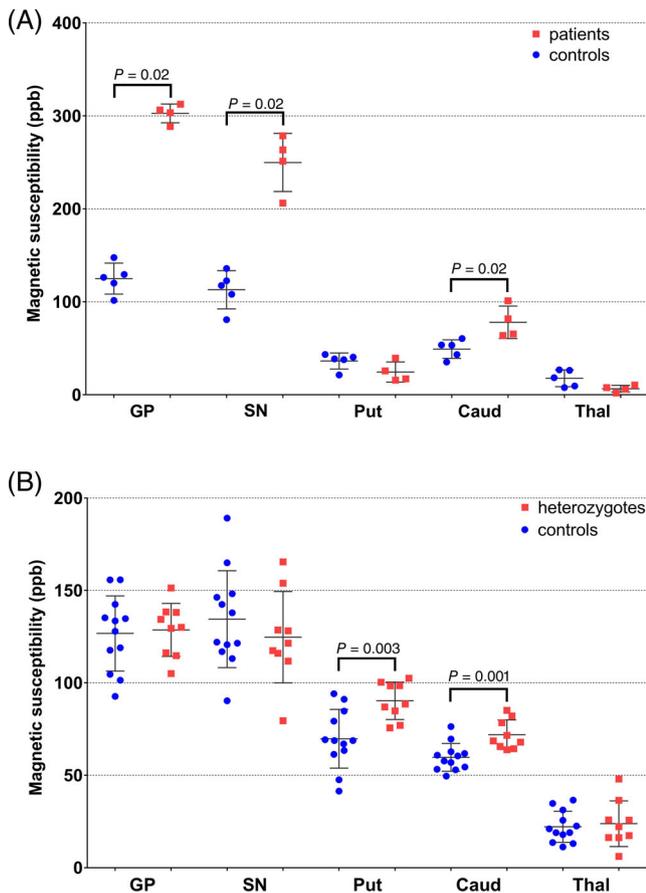
FIG. 3. Magnetic susceptibility in all examined ROIs in (A) MPAN homozygotes and (B) heterozygotes compared to age-matched healthy controls. Dots represent individual values of each subject; horizontal lines represent group means and standard deviations. Statistically significant differences with *P* values are denoted. ppb, parts per billion. [Color figure can be viewed at wileyonlinelibrary.com]

were significantly smaller compared to age-matched controls (Supporting Information Table S1).

MRS

Localized shimming resulted in water linewidths of 11.4 ± 0.9, 11.4 ± 0.9, and 12.2 ± 0.4 Hz for controls, heterozygotes, and patients, respectively. The high signal-to-noise ratio (SNR) of the spectra, exemplified in Figure 4, allowed the quantification of 13 individual and five combined metabolites with Cramér-Rao lower bounds (CRLBs) <20% for all three groups, including gamma-aminobutyric acid, glutamine (Gln), glutamate (Glu), and lactate (Lac). Metabolite quantification with CRLB lower than 20% are often deemed as reliable, although for metabolites with inherently low concentrations, such a threshold should be applied with caution.[24] Comparing patients and controls revealed significant increases ($P = 0.009$) in Glu, taurine (Tau), and the combined concentration of Glu + Gln in the patient group. No significant differences between heterozygotes and controls were detected, except for a statistical trend in total choline levels (tCho). Mean metabolite concentrations obtained from heterozygotes and controls are shown as well as the individual results of the MPAN patients in Supporting Information Table S2.

Discussion

In this ultrahigh field MR study, we utilized QSM to quantify iron content in the basal ganglia and thalamus and MRS of WM to characterize the metabolic footprint of MPAN patients and asymptomatic heterozygous
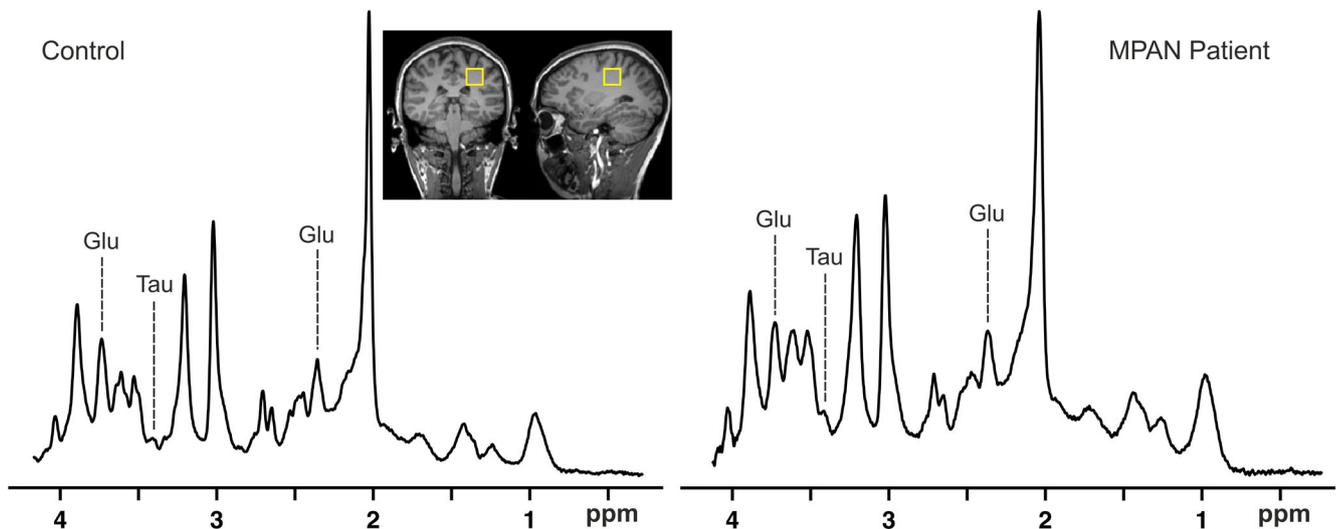
FIG. 4. ^{1}H MR spectra from a VOI in the precentral/postcentral WM (inset) acquired at 7T with the SPECIAL sequence (TR/TE = 9,000/11 ms) for an age-matched control (left) and a MPAN patient (right). Metabolites with significant concentration changes are indicated. Note the high SNR and comparable data quality of the two data sets. ppm, parts per million. [Color figure can be viewed at wileyonlinelibrary.com]

C19orf12 gene mutation carriers in contrast to healthy controls of comparable age.

MPAN Findings

A 2- to 3-fold increase of magnetic susceptibility strongly suggests an increase in iron content in the GP and SN of MPAN patients compared to controls. Compared to the pattern of iron accumulation in PKAN, which is largely confined to the GP and SN,[25,26] in MPAN we also observed an abnormality in the caudate nucleus; less pronounced, but also consistent with iron deposition. Additionally, atrophy of the caudate nucleus found in patients supports involvement of this structure in MPAN. It is worth noting, however, that structural atrophy could theoretically affect the measured local susceptibilities. It is unclear whether the loss of soft tissue as a whole or of diamagnetic myelin specifically dominates this interaction. Nonetheless, it is widely accepted that susceptibility measurements are somewhat confounded by regional gray matter atrophy. In this study, however, we detected early susceptibility changes in the caudate nucleus and putamen of heterozygous mutation carriers in the absence of detectable atrophy, suggesting that iron deposition may be an upstream event preceding cell loss in the caudate nucleus of MPAN patients. Previous studies in MPAN using clinical MRI at 3.0 T showed caudate iron accumulation only in late-onset or long-standing cases.[5] In this study, taking advantage of the enhanced sensitivity to iron-induced field inhomogeneities at ultrahigh magnetic field strengths, we have shown that caudate nucleus iron accumulation is a common feature of MPAN patients with typical age at onset and relatively short disease duration. None of the patients displayed an "eye-of-the-tiger sign," which is considered to be pathognomonic of PKAN, but has also been observed, albeit in a less pronounced form, in MPAN.[27,28]

We observed slight metabolite concentration differences between patients and controls in the corticospinal tracts. Caution should be exercised, however, when interpreting these findings, because of the limited number of examined patients. The increase in Tau levels might be partially attributed to the relatively young age of the patient group compared to controls, given that taurine decreases with age.[29] On the other hand, increased Glu levels in MPAN patients may be related to a dysfunctional regulation of excitatory neuron-glia transmission[30] along fibers of the motor pathway, which could thus explain the predominant spastic-paretic phenotype in MPAN. It is well established that vesicular Glu release from the axons in WM contributes to action-potential propagation.[31] It has been also documented that chronically increased glutamatergic release from central nervous system (CNS) axons may lead to myelin damage.[32] Increased Glu detectable by MRS in earlier disease stages may thus precede the

macroscopic WM lesions often observed in MPAN patients with long-standing disease.[7] Atrophy of the thalamus and striatum detected by the volumetric analysis further confirms that MPAN affects not only GP and SN, but also causes global CNS abnormalities.

Previous MRS studies showed abnormal cerebral Glu concentration in various diseases, such as schizophrenia, hepatic encephalopathy, and migraine.[33,34] Other NBIA subtypes have also been studied using MRS. Interestingly, increased Glu/Gln compound levels were also observed in the periventricular WM in PKAN patients.[35] It is thus possible that increased Glu levels in WM is a common finding across NBIA disorders or even more likely an unspecific marker of dysfunctional transmission along WM tracts in general. These MRS studies cannot be directly compared; therefore, it remains to be elucidated whether greater pyramidal Glu levels in MPAN compared to PKAN could explain the prominent spastic paresis heralding the former disorder.

Investigation of Heterozygotes

This study also aimed to ascertain whether asymptomatic, non-manifesting relatives with heterozygous gene mutations show subtle neuroradiological and/or -chemical abnormalities (i.e., signs of iron accumulation or metabolic changes) that could serve as endophenotypic markers. The precedent to this hypothesis are mild abnormalities identified in heterozygous gene mutation carriers of other recessive movement disorders, such as Parkin- or PINK1-related parkinsonism.[36,37] Confirming our hypothesis, this study detected statistically significant changes in striatal iron levels in heterozygotes, whereas the metabolic pattern measured by MRS was not statistically different from that in controls. Regression analysis of age and magnetic susceptibility showed similar slope, but significantly higher y-intercept, in heterozygotes compared to controls, suggesting that striatal iron levels are elevated in heterozygotes from a relatively young age. This is in contrast to PKAN, the most common NBIA variant, where brain iron content was within normal limits in heterozygous mutation carriers.[25,26]

Interestingly, heterozygous *C19orf12* gene mutation carriers showed higher iron content in the striatum, but not in GP and SN, which are the primary sites of iron depositions in homozygotes. This, together with the finding of increased magnetic susceptibility and accelerated atrophy in the caudate nucleus in MPAN patients, suggests that the striatum could be the primary site of iron accumulation and disease pathology, whereas the GP might be a downstream "sink" where iron is ultimately deposited. It is, however, not clear why increased iron was not observed in the putamen in MPAN patients, particularly when putaminal atrophy

was detected in this group. A possible explanation is that the putamen is directly adjacent to the GP, and therefore its associated signal is at greater risk of contamination by the nonlocal effect of magnetic field disturbances caused by the high levels of GP iron in MPAN. This conceivable scenario warrants a future technical investigation. Direct measurement of iron concentrations in ex vivo tissue could provide an independent ground truth to address this question. Absence of movement disorders in 8 of 9 examined heterozygotes suggests that increased iron levels alone may not be clinically significant. However, we only performed routine clinical examination without any quantitative motor or cognitive testing. Minor cognitive and motor deficits cannot be ruled out in C19orf12 heterozygotes given that previous studies have shown correlations between higher iron content in the putamen and GP and worse cognitive and motor function in healthy elderly subjects[38,39] and found evidence of elevated iron content preceding atrophy in the putamen.[40] Higher variability of cerebral iron concentration in elderly subjects has been described previously,[41] though its causes remain largely unknown.[42] Our results suggest that genetic factors may, at least to some extent, underlie this variability.

Several limitations should be noted. Most important, it is the small number of patients that could be included because of the low prevalence of MPAN and strict rules for using ultrahigh field MRI. Of note, despite that we have not used multiple comparison correction, the results are still robust for major findings; the statistical significance of higher magnetic susceptibility in heterozygotes compared to controls survives the conservative Bonferroni correction for the family of five tests yielding corrected threshold of $P < 0.01$. Additionally, statistical significance of higher magnetic susceptibility in the caudate nucleus in MPAN patients compared to controls is also below the Bonferroni-corrected P-value threshold for three tests ($P < 0.017$); three tests are considered given that higher iron content in the GP and SN in MPAN patients is well known, so the statistical analysis in these two ROIs can be regarded as formal and confirmatory. Also, it is not clear whether magnetic susceptibility is linearly related to iron concentrations under the circumstances of heavy iron deposition as is the case in NBIA. Nevertheless, nonlinear relation between magnetic susceptibility and iron content would not derogate significant differences found in this study. Spatial distortions are also a known issue of ultrahigh field MRI. Although we made an effort to minimize them by segmenting deep gray matter nuclei simultaneously on MPRAGE and QSM images, volumetric results must be interpreted with caution and warrant a future investigation.

In conclusion, compared to healthy subjects, MPAN patients consistently display not only increased iron in the GP and SN, but also in the caudate nucleus along with metabolic changes in the corticospinal pathway. Our findings imply that heterozygosity leads to subtle iron accumulation in the striatum, even in the absence of overt neurological signs. ∎

References

1. Schneider SA, Dusek P, Hardy J, Westenberger A, Jankovic J, Bhatia KP. Genetics and pathophysiology of neurodegeneration with brain iron accumulation (NBIA). Curr Neuropharmacol 2013;11:59–79.
2. Hartig MB, Iuso A, Haack T, et al. Absence of an orphan mitochondrial protein, c19orf12, causes a distinct clinical subtype of neurodegeneration with brain iron accumulation. Am J Hum Genet 2011;89:543–550.
3. Venco P, Bonora M, Giorgi C, et al. Mutations of C19orf12, coding for a transmembrane glycine zipper containing mitochondrial protein, cause mis-localization of the protein, inability to respond to oxidative stress and increased mitochondrial Ca(2)(+). Front Genet 2015;6:185.
4. Hogarth P, Gregory A, Kruer MC, et al. New NBIA subtype: genetic, clinical, pathologic, and radiographic features of MPAN. Neurology 2013;80:268–275.
5. Gore E, Appleby BS, Cohen ML, et al. Clinical and imaging characteristics of late onset mitochondrial membrane protein-associated neurodegeneration (MPAN). Neurocase 2016;22:476–483.
6. Selikhova M, Fedotova E, Wiethoff S, et al. A 30-year history of MPAN case from Russia. Clin Neurol Neurosurg 2017;159:111–113.
7. Skowronska M, Kmiec T, Jurkiewicz E, Malczyk K, Kurkowska-Jastrzebska I, Czlonkowska A. Evolution and novel radiological changes of neurodegeneration associated with mutations in C19orf12. Parkinsonism Relat Disord 2017;39:71–76.
8. Kurian MA, Hayflick SJ. Pantothenate kinase-associated neurodegeneration (PKAN) and PLA2G6-associated neurodegeneration (PLAN): review of two major neurodegeneration with brain iron accumulation (NBIA) phenotypes. Int Rev Neurobiol 2013;110:49–71.
9. Dusek P, Skoloudik D, Roth J, Dusek P. Mitochondrial membrane protein-associated neurodegeneration: a case report and literature review. Neurocase 2018;24:161–165.
10. Lobel U, Schweser F, Nickel M, et al. Brain iron quantification by MRI in mitochondrial membrane protein-associated neurodegeneration under iron-chelating therapy. Ann Clin Transl Neurol 2014;1:1041–1046.
11. Deistung A, Schweser F, Reichenbach JR. Overview of quantitative susceptibility mapping. NMR Biomed 2017;30. https://doi.org/10.1002/nbm.3569. Epub 2016 Jul 19.
12. Duarte JM, Lei H, Mlynarik V, Gruetter R. The neurochemical profile quantified by in vivo 1H NMR spectroscopy. NeuroImage 2012;61:342–362.
13. Mekle R, Mlynarik V, Gambarota G, Hergt M, Krueger G, Gruetter R. MR spectroscopy of the human brain with enhanced

signal intensity at ultrashort echo times on a clinical platform at 3T and 7T. Magn Reson Med 2009;61:1279–1285.

14. Tkac I, Oz G, Adriany G, Ugurbil K, Gruetter R. In vivo 1H NMR spectroscopy of the human brain at high magnetic fields: metabolite quantification at 4T vs. 7T. Magn Reson Med 2009;62:868–879.

15. Parker DL, Payne A, Todd N, Hadley JR. Phase reconstruction from multiple coil data using a virtual reference coil. Magn Reson Med 2014;72:563–569.

16. Acosta-Cabronero J, Milovic C, Mattern H, Tejos C, Speck O, Callaghan MF. A robust multi-scale approach to quantitative susceptibility mapping. Neuroimage 2018;183:7–24.

17. Sanfilipo MP, Benedict RH, Zivadinov R, Bakshi R. Correction for intracranial volume in analysis of whole brain atrophy in multiple sclerosis: the proportion vs. residual method. Neuroimage 2004;22: 1732–1743.

18. Mlynarik V, Gambarota G, Frenkel H, Gruetter R. Localized short-echo-time proton MR spectroscopy with full signal-intensity acquisition. Magn Reson Med 2006;56:965–970.

19. Tkac I, Starcuk Z, Choi IY, Gruetter R. In vivo 1H NMR spectroscopy of rat brain at 1 ms echo time. Magn Reson Med 1999;41: 649–656.

20. Brown MA. Time-domain combination of MR spectroscopy data acquired using phased-array coils. Magn Reson Med 2004;52: 1207–1213.

21. Provencher SW. Estimation of metabolite concentrations from localized in vivo proton NMR spectra. Magn Reson Med 1993;30:672–679.

22. Cudalbu C, Mlynarik V, Gruetter R. Handling macromolecule signals in the quantification of the neurochemical profile. J Alzheimers Dis 2012;31(Suppl 3):S101–S115.

23. Jenkinson M, Beckmann CF, Behrens TE, Woolrich MW, Smith SM. Fsl. Neuroimage 2012;62:782–790.

24. Kreis R. The trouble with quality filtering based on relative Cramer-Rao lower bounds. Magn Reson Med 2016;75:15–18.

25. Delgado RF, Sanchez PR, Speckter H, et al. Missense PANK2 mutation without "eye of the tiger" sign: MR findings in a large group of patients with pantothenate kinase-associated neurodegeneration (PKAN). J Magn Reson Imaging 2012;35:788–794.

26. Dusek P, Tovar Martinez EM, Madai VI, et al. 7-Tesla magnetic resonance imaging for brain iron quantification in homozygous and heterozygous PANK2 mutation carriers. Mov Disord Clin Pract 2014;1:329–335.

27. Yoganathan S, Sudhakar SV, Thomas M, Dutta AK, Danda S. "Eye of tiger sign" mimic in an adolescent boy with mitochondrial membrane protein associated neurodegeneration (MPAN). Brain Dev 2016;38:516–519.

28. Skowronska M, Kmiec T, Kurkowska-Jastrzebska I, Czlonkowska A. Eye of the tiger sign in a 23 year patient with mitochondrial membrane protein associated neurodegeneration. J Neurol Sci 2015;352:110–111.

29. Govindaraju V, Young K, Maudsley AA. Proton NMR chemical shifts and coupling constants for brain metabolites. NMR Biomed 2000;13:129–153.

30. Westergaard N, Sonnewald U, Schousboe A. Metabolic trafficking between neurons and astrocytes: the glutamate/glutamine cycle revisited. Dev Neurosci 1995;17:203–211.

31. Kukley M, Capetillo-Zarate E, Dietrich D. Vesicular glutamate release from axons in white matter. Nat Neurosci 2007;10:311–320.

32. Doyle S, Hansen DB, Vella J, et al. Vesicular glutamate release from central axons contributes to myelin damage. Nat Commun 2018;9:1032.

33. Ramadan S, Lin A, Stanwell P. Glutamate and glutamine: a review of in vivo MRS in the human brain. NMR Biomed 2013;26: 1630–1646.

34. Zielman R, Wijnen JP, Webb A, et al. Cortical glutamate in migraine. Brain 2017;140:1859–1871.

35. Hajek M, Adamovicova M, Herynek V, et al. MR relaxometry and 1H MR spectroscopy for the determination of iron and metabolite concentrations in PKAN patients. Eur Radiol 2005;15: 1060–1068.

36. Binkofski F, Reetz K, Gaser C, et al. Morphometric fingerprint of asymptomatic Parkin and PINK1 mutation carriers in the basal ganglia. Neurology 2007;69:842–850.

37. Schneider SA, Talelli P, Cheeran B, et al. Motor cortical physiology in patients and asymptomatic carriers of parkin gene mutations. Mov Disord 2008;23:1812–1819.

38. Ghadery C, Pirpamer L, Hofer E, et al. R2* mapping for brain iron: associations with cognition in normal aging. Neurobiol Aging 2015; 36:925–932.

39. Daugherty AM, Raz N. Appraising the role of iron in brain aging and cognition: promises and limitations of MRI methods. Neuropsychol Rev 2015;25:272–287.

40. Daugherty AM, Raz N. Accumulation of iron in the putamen predicts its shrinkage in healthy older adults: a multi-occasion longitudinal study. Neuroimage 2016;128:11–20.

41. Hallgren B, Sourander P. The effect of age on the non-haemin iron in the human brain. J Neurochem 1958;3:41–51.

42. Pirpamer L, Hofer E, Gesierich B, et al. Determinants of iron accumulation in the normal aging brain. Neurobiol Aging 2016;43: 149–155.

43. Deschauer M, Gaul C, Behrmann C, Prokisch H, Zierz S, Haack TB. C19orf12 mutations in neurodegeneration with brain iron accumulation mimicking juvenile amyotrophic lateral sclerosis. J Neurol 2012;259:2434–2439.

44. Schottmann G, Stenzel W, Lutzkendorf S, Schuelke M, Knierim E. A novel frameshift mutation of C19ORF12 causes NBIA4 with cerebellar atrophy and manifests with severe peripheral motor axonal neuropathy. Clin Genet 2014;85:290–292.

Supporting Data

Additional Supporting Information may be found in the online version of this article at the publisher's web-site.